

Numerical Modelling and Validation of Induction Melting of IN713C for Investment Casting

V U Thomas¹, M A Yar¹, J C T Cullen¹, S Mehraban¹, S G R Brown¹, N P Lavery¹

1. College of Engineering, Swansea University, Swansea, Wales, United Kingdom

Abstract: Investment casting is practised in both the automotive and aerospace industries, to produce casted components where a high-quality surface finish is critical. Vacuum induction melting (VIM) and direct pouring into an investment casting shell mould is an advantageous manufacturing technique, due to the speed at which casting trees with a high yield can be produced. However, variables introduced in the VIM process can affect the resultant temperature and velocity profiles of the alloy during induction heating, melting and subsequent pouring. An understanding of induction heating and melting is invaluable in determining the effect of these variables upon the quality of the finished castings. Numerical modelling of the induction heating and melting process is vital in developing this understanding. Data on measured temperatures of an Inconel 713C (IN713C) billet in a small-scale induction melting experiment during heating and cooling cycles were recorded using an optical pyrometer. The billet was heated and melted using an induction coil, followed by cooling as the coil power was switched off. This cycle was repeated, with heating and cooling curves plotted with respect to time. The ability to accurately model the heating, melting, and cooling of an IN713C billet on a smaller scale, provides a solid foundation for modelling VIM investment casting on a larger industrial scale. Development of an experimentally validated, accurate induction melting model paves the way to a greater understanding of the VIM process for the application of component production in the automotive and aerospace industries. Principles from the model can be applied to a larger scale model, providing an effective tool to investigate the effect of variables such as alloy condition on the quality and yield of finished castings.

Keywords: Phase Change, Heat Transfer, Electromagnetics, COMSOL, Differential Scanning Calorimetry, Induction Coil, Optical Pyrometer, Crucible, Billet, Electromagnetic Stirring, Emissivity, Simulation, Turbulence, Fluid Flow.

1 Introduction

Induction melting is a phenomena which occurs when an electrically conductive metal is placed within an induction coil. The induction coil produces an alternating current (AC), which in turn produces a changing magnetic field with a frequency matching the AC in the surrounding area. Inductive heating occurs by the Joule effect. Eddy currents of the same frequency as the coil current, but in the opposing direction are induced in the metal [1]. IN713C is a nickel based superalloy. Inconels are considered to be paramagnetic [2]. This means that they are comprised of many small particles which can

become magnetised by an externally applied field. The particles align with the field polarity, and become polarised with a north and south pole. The field polarity changes many times per second due to the AC, which causes the magnetic particles to realign themselves with the changing field polarity. Resistance within the metal causes intermolecular friction, which dissipates as heat [3]. The AC is applied until the metal becomes molten.

COMSOL was used to model the induction heating, melting, and cooling which was experimentally observed in the billet. The AC/DC module was used to implement the induction coil, producing the electromagnetic field in a 2D axisymmetric Frequency-Transient study. Phase Change Material functionality was used to map the progression of alloy phase change throughout the heating, melting and cooling cycles. Melting temperature, phase transition interval and latent heat of fusion for IN713C were determined using data from a Differential Scanning Calorimeter (DSC). Emissivity of IN713C was required for the numerical model, and obtained experimentally. Temperature results from the conductive heat transfer models were compared to experimentally obtained temperature data during heating, melting and cooling cycles. A model including Fluid Flow functionality, using a Low Reynolds number $k-\epsilon$ turbulence model, was used to model the effect of eddy currents. The time-averaged Lorentz force was applied to the fluid to drive the molten metal in electromagnetic stirring. A source term, F , was prescribed to dampen the velocity at the phase-change interface, so that velocities produced by solution of the momentum equations were inhibited for alloy in a solid state. Velocity profiles generated due to electromagnetic stirring provided qualitative information for the eddy currents, and a model with phase change and fluid flow will be developed upon in further work.

2 Experimental Methods and Results

2.1 Differential Scanning Calorimetry

Differential Scanning Calorimetry is a thermal analysis technique, which measures heat flows and temperatures for exothermic and endothermic transitions. Conducting DSC experiments prior to induction melting was useful for determining the temperature at which the sample was fully molten, while phase change temperature transition interval and latent heat of fusion were important parameters for use in the numerical model. A DSC 404 F1 Pegasus High-Temperature machine was used to establish the phase transformations, solidus and liquidus temperatures, and specific heat capacity of

IN713C. The DSC acquires this data by using thermocouples to detect heat flow differences between a sample inside an alumina crucible, and an empty reference crucible. An initial cycle was conducted with an empty crucible on the platinum head alongside the reference crucible. This allowed for any corrections to be made, forming a baseline for the following experiments. Once this corrective run was complete, a sample of IN713C was subjected to cyclic heating and cooling in the DSC under nitrogen gas. The sample was heated to 1500°C at a rate of 20 K/min, held in an isothermal state for five minutes, and cooled to 50°C at a rate of 20 K/min. This process was repeated three times. The third measurement, shown in Figure 1, was considered to be the most accurate.

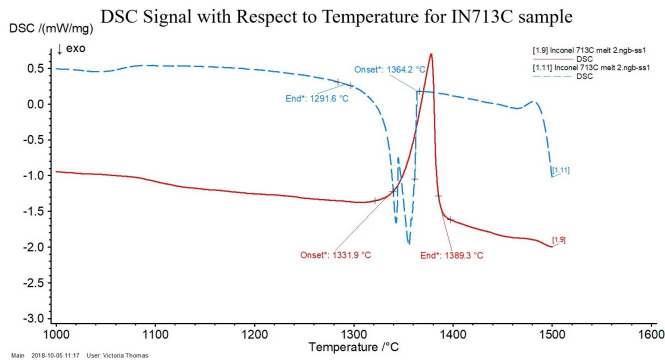


Figure 1: DSC heating and cooling curves for IN713C

DSC signal analysis showed solidus and liquidus temperatures from the onset and end of peaks. It is customary to use the heating curve to read solidus and liquidus temperatures [4]. Solidus temperature can be identified as the first deviation from the baseline of the heating curve, shown in red on Figure 1. Liquidus temperature can be defined at the point of return to the baseline upon heating. From the heating curve, solidus temperature is 1389.3°C and liquidus temperature is 1331.9°C. The temperature transition interval and latent heat of fusion were 57.4 K and 333 kJ/kg respectively. Peaks are recorded at lower values on the cooling curve, which is a result of the undercooling effect [5]. As the start and end points of peaks are subjective, this is a limitation that can cause variability in accuracy of solidus and liquidus temperatures.

2.2 Induction Heating and Melting

A 20 mm long, 12 mm diameter IN713C billet was heated in a ceramic crucible using an EasyHeat 0224FF CE 2.4 kW induction heater, in an argon environment inside a Saffron Scientific Equipment anaerobic glove box. The billet was inserted into the crucible and placed on a boron nitride plate. The plate was adjusted to a height which allows the crucible to sit within the coil using a jack stage. Temperature of the top billet face was measured using an Optris CTLaser 2MH CF3 optical pyrometer, which is capable of measuring temperatures in the range of 385-1600°C. The optical pyrometer was fixed above the sample as shown in the experimental setup diagram, Figure 2. An alignment laser ensured that the top face of the

billet was being measured by the optical pyrometer. Initial heating and melting experiments were conducted to determine the best current set points to use.

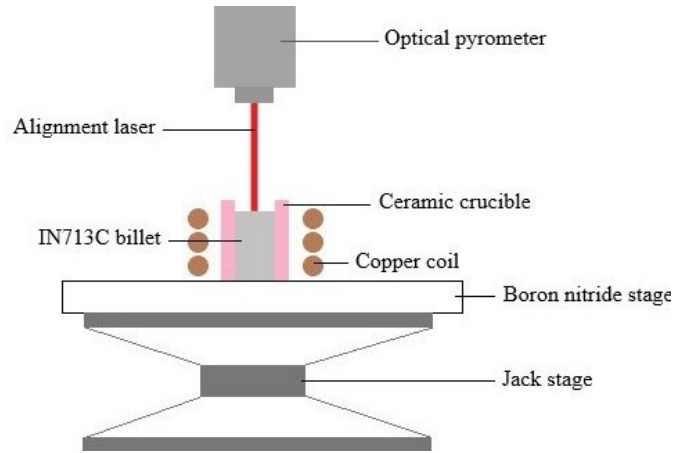


Figure 2: Induction melting and optical pyrometer set-up

A heating experiment involved heating the billet to over 900°C, by setting the induction heater current to 100.1 A. As billet temperature started to plateau, the current was increased to 140.4 A. Once it reached a maximum temperature of 944.1°C, the current was set to zero. The sample was allowed to cool until it reached the bottom of the optical pyrometer temperature measurement range.

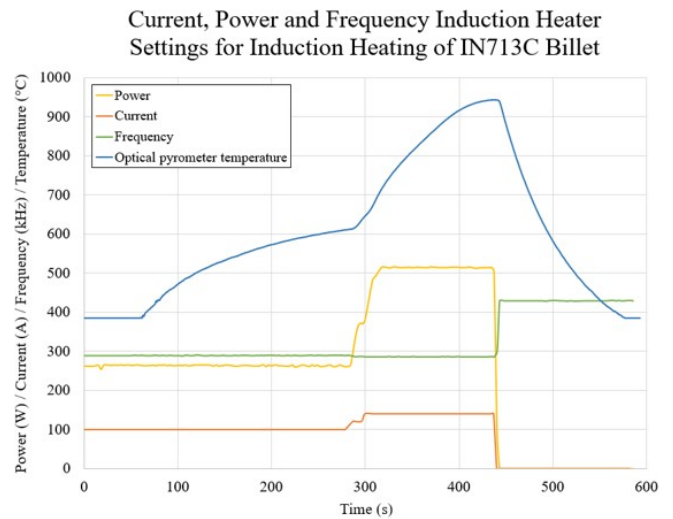


Figure 3: Temperature reading and induction heater settings: heating

Induction melting of the billet for a fixed high current required thermal cycling of the sample in the crucible, to prevent crucible breakage due to thermal shock. After initial thermal cycling, induction melting of the billet was achieved by setting the induction heater current to 280.1 A. The current was held at this value until the billet reached a maximum temperature of 1372.9°C. Once the sample was observed to be molten, the current was set to zero. The sample was allowed to cool until it reached the bottom of the optical pyrometer

temperature measurement range. For both heating and melting experiments, the optical pyrometer emissivity value was fixed at 1.00. Emissivity was set to this value, as the dimensions and setup of the measurement target were such that it could be approximated as a black body for temperature measurement purposes, where the emissivity of a black body is 1.00.

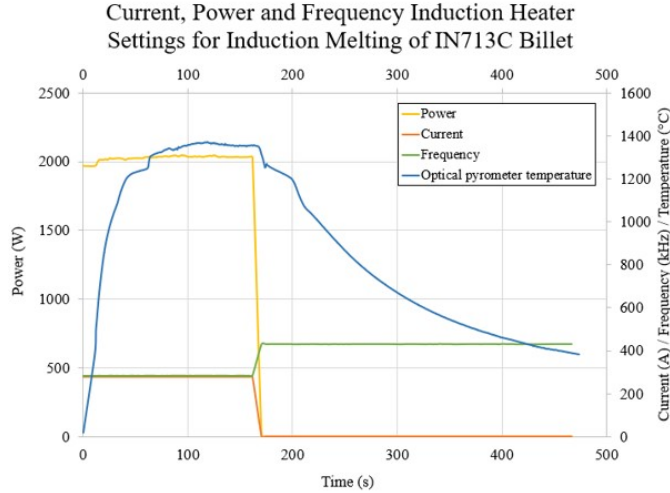


Figure 4: Temperature reading and induction heater settings: melting

Temperature data from optical pyrometer measurements for the induction heating and melting experiments are shown in Figures 3 and 4 respectively. The optical pyrometer system accuracy is $\pm(0.3\%T_{meas}+2)^{\circ}\text{C}$, where T_{meas} is the measured temperature. Current, frequency and power settings for the induction heater were recorded for both heating and melting experiments, and are also shown in the graphs.

2.3 Emissivity Measurement

Emissivity values for pure metals and commonly used materials can be found in existing literature. However, emissivity data on specific alloys such as IN713C are not often available in literature due to the vast number of existing alloys. In addition, emissivity is not solely dependent on material, but other factors such as surface finish. Therefore, experimental measurement of emissivity was required. The emissivity of IN713C was determined using a box furnace to heat a billet, comparing temperature readings from the infrared thermometer to the thermocouple reading for a fixed emissivity value [6]. A 50 mm long, 50 mm diameter IN713C billet with a notch cut in the curved edge face was heated in a Nabertherm box furnace, for temperatures up to 1100°C. This ensured the sample was kept within a temperature range that would not allow the sample to become molten. An N-type wire thermocouple was placed in the billet notch, connected to a data logger via the back port of the furnace. The N-type was chosen for its suitability for high temperature applications, while experiencing a lesser degree of drift in oxidising atmospheres compared to K-type thermocouples. An Endurance 1RL F2 2-Colour Infrared Thermometer was bolted to a jack stage, with

the lens positioned 600 mm from the billet front face. The distance ratio for the infrared thermometer is 100:1, therefore at 600 mm the diameter of the target spot size was 6 mm. The lens was focused such that the target position did not shift with eye movement. The emissivity value was set within the Endurance infrared thermometer software. It was set at 0.85, as according to the equipment manufacturer the emissivity for oxidised nickel is between 0.8-0.9 [7].

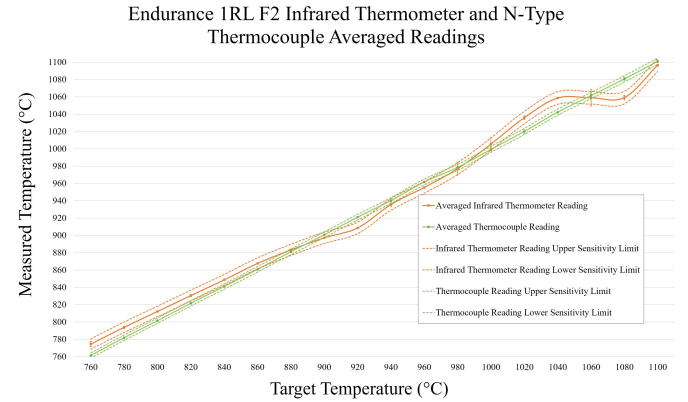


Figure 5: Temperature measurement comparisons, emissivity = 0.85

The sample was heated in 20°C intervals from 760-1100°C. Temperature readings were taken by opening the furnace door, which allowed the infrared thermometer to read the temperature of the billet front face. Infrared thermometer measurements were compared with thermocouple temperature readings taken at the same time. This experiment was repeated three times for the chosen temperature range. Temperature measurements from three repeated experiments for determining temperature measurement accuracy at an emissivity setting of 0.85 for IN713C, were averaged and plotted in Figure 5.

3 COMSOL Modeling

3.1 Governing Equations and Physics

3.1.1 Induction Heating

The ‘Electromagnetic Heating’ Multiphysics interface was applied, involving a combination of the ‘Magnetic Fields’ and ‘Heat Transfer in Solids’ physics nodes. A fully coupled solver approach was adopted, for a Frequency-Transient model. A transient magnetic field is produced by applying an AC to a coil, which induces eddy currents in nearby electrically conductive materials according to Maxwell’s equations. These equations describe the relationship between fundamental electromagnetic quantities [8]. Maxwell-Ampere’s law for general time-varying fields can be written as:

$$\nabla \times \mathbf{H} = \mathbf{J} + \frac{\partial \mathbf{D}}{\partial t} \quad (1)$$

where \mathbf{H} is magnetic field intensity, \mathbf{J} is current density, and \mathbf{D} is electric displacement or electric flux density. Faraday’s law

can be written as:

$$\nabla \times \mathbf{E} = -\frac{\partial \mathbf{B}}{\partial t} \quad (2)$$

where \mathbf{E} is electric field intensity and \mathbf{B} is magnetic flux density. Equation 3 is the electric form of Gauss' law, where ρ is electric charge density. Equation 4 is Gauss' law in the magnetic form.

$$\nabla \cdot \mathbf{D} = \rho \quad (3)$$

$$\nabla \cdot \mathbf{B} = 0 \quad (4)$$

Heat generation from induced currents in the electrically conductive material due to the Joule effect can be described by the following equation, where P is power, I denotes current and R is resistance:

$$P = I^2 R \quad (5)$$

The Lorentz force can be accurately calculated for an electrically conductive material, and added as a source term to the fluid momentum equation:

$$\mathbf{F}^{\text{Lorentz}} = \mathbf{J} \times \mathbf{B} \quad (6)$$

Skin depth is also an important factor in modelling penetration of a magnetic field within an electrically conductive material. Penetration depth decreases as frequency of the AC increases, as shown in Equation 7 [9]:

$$\delta = \frac{1}{\sqrt{\pi f \mu \sigma}} \quad (7)$$

where δ is skin depth in metres, f is frequency of the alternating current in Hz, μ is absolute permeability in H/m, and σ is electrical conductivity in S/m.

3.1.2 Mushy Region Phase Change

'Phase Change Material' functionality was used in models both with and without fluid flow, to input the relevant parameters regarding material phase change. However, for the model including fluid flow the 'Nonisothermal Flow' Multiphysics interface was applied for the fluid flow model, employing a $k-\epsilon$ turbulence model. Materials undergoing phase change with a 'mushy' region have a temperature transition interval over which the phase change takes place. Activation of velocities across the mushy region can be modelled by setting permeability as a function of porosity. A damping source term, F , was applied:

$$F_{r,z} = -\frac{(1-\lambda)^2}{\lambda^3 + q} C(u, w) \quad (8)$$

where λ is the liquid phase volume fraction, C is a physics dependent large constant to produce damping, and q is a sufficiently small constant to avoid division by zero. u and w are the fluid velocity components in two directions for the 2D model. Equation 8 was taken from the method of modelling convection-diffusion for mushy region phase change problems

using a fixed grid approach by Voller et al. [10]. For the qualitative model with fluid flow, C was set to 1600 kg/m³s and q was equal to 0.001. These values were chosen to replicate parameters in the referenced paper.

3.2 Model Setup

3.2.1 Geometry and Mesh

The model geometry was comprised of several domains, using a 2D axisymmetric approach. An infinite elements domain was applied around the outside of the argon domain. Figure 6 shows the model geometry with labelled domains for the billet, coil, ceramic crucible and argon, alongside the mesh configuration.

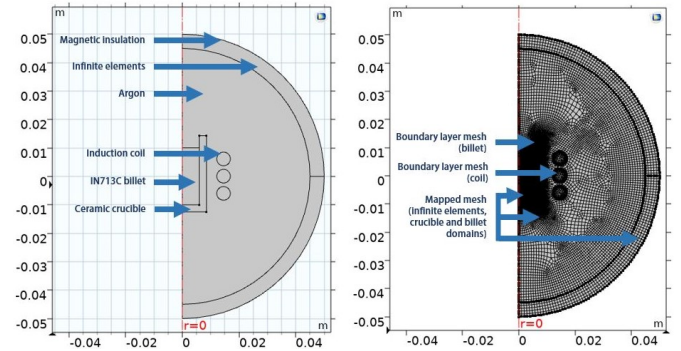


Figure 6: 2D axisymmetric model geometry and mesh

A mapped mesh with quad elements was applied to the infinite elements, crucible and billet domains. A free quad mesh was applied to the argon domain. Triangular elements covered the centre of the coil domains, with boundary layers on the boundaries of the billet and coil domains. The boundary layer mesh type was applied to ensure that a sufficient number of elements covered the total skin depth. Convention dictates that a minimum of four elements should cover the skin depth [11].

Table 1: Calculated penetration depths at known frequencies

Material	Frequency (kHz)	Skin Depth (mm)
Copper	282	0.12237
	429	0.09922
IN713C	282	1.13767
	429	0.92238

Therefore, five elements were applied across the calculated skin depth for each conductor material. The calculated skin depths for copper and IN713C at the frequencies recorded from the induction heater are listed in Table 1. Skin depths for the known frequencies determined the size of boundary layers.

3.3 Boundary Conditions

Magnetic insulation is a homogeneous Dirichlet boundary condition, which fixes the field variable which is being solved for as zero at the boundary [12]. The magnetic insulation was applied to the outside of the infinite elements domain, to ensure

that it was far away enough from the induction coil and billet such that the solution was unaffected, and boundary conditions could be applied. The infinite elements domain was applied as a method for limiting the size of the argon domain, by applying coordinate scaling to an outer virtual domains layer. The three turn coil was represented by the COMSOL Coil feature from the AC/DC module, applied to the three circular domains. The ‘Single conductor’ option was used, modelling the solid regions as a ‘Coil group’. The current of the coil corresponded to the integral of the current density on a cross section. As the current varied with time for the induction heating model, it was defined as a time dependent piecewise cubic interpolation. ‘Surface-to-Ambient Radiation’ was applied to the billet top face, with the experimentally obtained surface emissivity of 0.85. An effective heat transfer coefficient was applied to all crucible surfaces exposed to the surrounding argon, as a ‘Heat Flux’. This artificially high effective heat transfer coefficient accounted for heat losses due to natural convection, radiative and other sources. Values between 50 - 5,000 W/m²K were tested in the model to determine which value most effectively captured sample cooling rate.

3.4 Material Properties

Temperature dependent material properties for IN713C were available in the materials library of COMSOL Multiphysics software. These temperature dependent relationships were described by piecewise functions over a given temperature range. Outside of the function range, COMSOL sets the properties to a constant value at the lower and upper ends of the piecewise function by default. The main model discussed in this paper used only conductive heat transfer without a fluid flow component, not accounting for natural convection. Artificially high values for effective thermal conductivity and effective specific heat capacity were employed at the melting point, to account for the liquid phase transition. The higher value accounts for a high rate of transport of momentum, as electromagnetic stirring generates strong fluctuating velocities with very strong convection [13]. The liquidus temperature, temperature transition interval and latent heat of fusion were required by the Phase Change Material functionality. Values for these material properties were taken from DSC data.

3.5 Fluid Flow

Quantitative temperature data was obtained from the solely heat conductive models in this paper. However, a qualitative model, for examining the behaviour of fluid flow as it initiates in an apple core pattern and stirs under electromagnetic forces, was developed. This model used a Frequency Domain study step to provide consistent initial conditions before deploying a time dependent Frequency Transient model. The Frequency Transient model used a segregated solver approach. Two types of ‘Volume Force’ were applied to the billet region of the model including fluid flow. A ‘Solid’ force, accounting for velocity damping in the solid and mushy regions, was applied by Equation 8 as described in subsection 3.1.2. To

account for buoyancy in the liquid metal, gravity was taken into account. A ‘Magnetic’ force was also applied by multiplying the parameters ‘mf.Fltzavr’ and ‘mf.FLTzavz’ by the COMSOL parameter for liquid phase. This allowed the Lorentz time averaged magnetic force to drive the movement of the molten metal in electromagnetic stirring. A condition of ‘No slip’ was applied to the crucible walls, with a pressure point constraint of 0 Pa applied to the bottom inner corner of the crucible. The billet top face was defined as an outlet with a pressure of 1 atm.

3.6 Mesh Sensitivity

Electromagnetic heating was only active in the billet domain, with heat transfer modelled in both the billet and crucible. For this reason, the mesh sensitivity study was performed in the billet and crucible domains as the thermal problem was only solved in these areas. To measure the average temperature of the billet top face, a boundary probe was applied. The mesh convergence study was conducted for the model replicating induction melting, as this covered a wider range of temperatures. A standard approach was used, reducing element sizes until results convergence was observed.

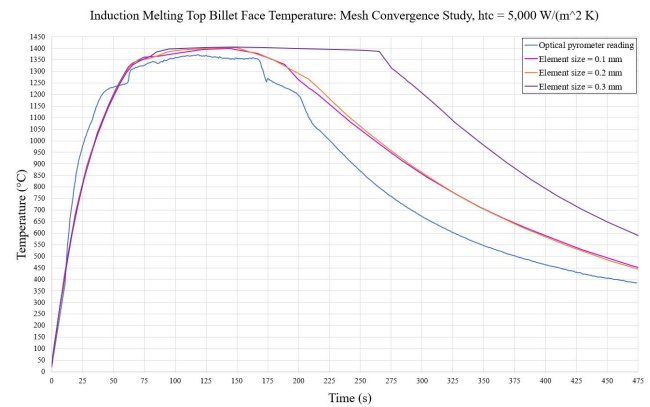


Figure 7: Mesh convergence study

Table 2: Relative CPU time and average model mesh element quality for varying billet and crucible domain max. element sizes

Element Length (mm)	CPU time	Element Quality
0.1	2.46	0.9596
0.2	1	0.9316
0.3	0.56	0.9241

Study results are shown in Figure 7, with maximum element length between 0.1-0.3 mm. An adaptive timestepping scheme was adopted, which allowed the software to automatically adjust the size of the timestep to remain within the relative tolerance of 0.01. The ‘Nonlinear controller’ option was selected, to account for the nonlinearity of the physics of this problem. CPU time relative to an element size of 0.2 mm and average mesh element quality for each element size is listed in Table 2. Results were converged to a satisfactory level for an element length of 0.2 mm. However, despite being 2.46 times

more computationally expensive than a maximum element length of 0.2 mm, total CPU time for 0.1 mm was acceptable. Therefore, for maximum accuracy all further results in this paper have been generated using maximum element length of 0.1 mm within the billet and crucible domains.

3.7 COMSOL Model Results

3.7.1 Heat Conductive Model

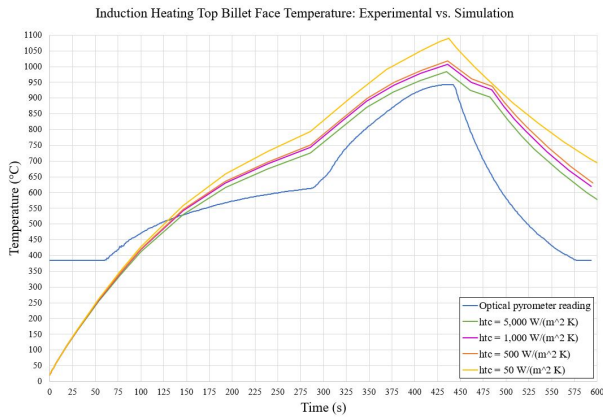


Figure 8: Induction heating simulation results for varying effective heat transfer coefficients

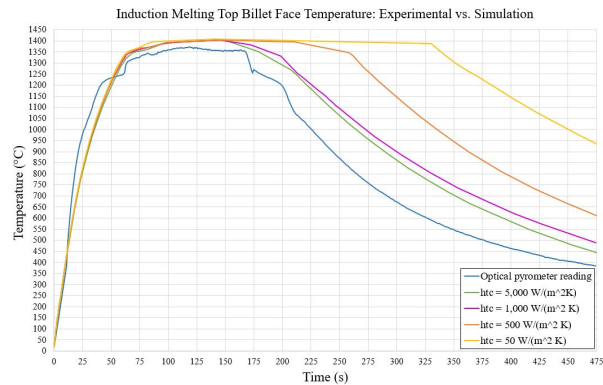


Figure 9: Induction melting simulation results for varying effective heat transfer coefficients

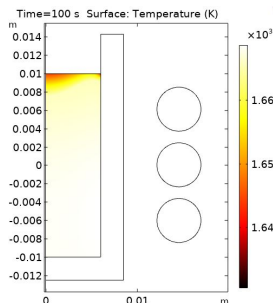


Figure 10: Billet temperature profile from melting model, $t = 100$ s

Induction heating and melting models for the solely heat conductive models were run for varying effective heat transfer coefficients, shown in Figures 8 and 9 respectively. Figure 10 shows the thermal profile of the billet at $t = 100$ s from the melting model, for a run where effective heat transfer coefficient was set as $5000 \text{ W/m}^2\text{K}$.

3.7.2 Fluid Flow Model

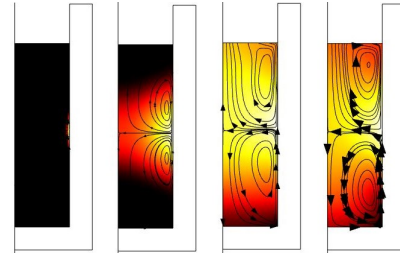


Figure 11: Phase transition and electromagnetic stirring

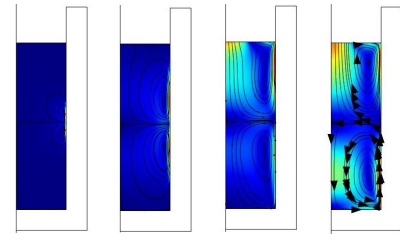


Figure 12: Velocity profile and electromagnetic stirring

For the qualitative fluid flow model, phase change transition and fluid flow driven by the Lorentz time averaged force can be seen in Figure 11, where a darker colour represents solid material and lighter areas represent the liquid phase. Magnitude controlled density streamlines are plotted, showing the velocity of the molten metal as it emerges at the liquid initiation site. Figure 12 shows the billet at identical timesteps with the same streamline plot, and velocity profile plotted on the billet domain surface. Blue represents lower velocities and red represents higher values.

4 Discussion

For both heating and melting models, an effective heat transfer coefficient of $5,000 \text{ W/m}^2\text{K}$ produced results which most closely matched the experimental results. Varying the values of effective heat transfer coefficient had a greater effect on cooling of the billet than heating. The temperature plot in Figure 10 showed that at $t = 100$ s, the centre part of the top piece of the billet remains cooler than the rest of the billet domain surface. It is known from the physics of induction melting that the top centre part of the billet remains solid until last, which is shown in Figure 13. This image was taken from a thermal imaging video which was recorded in an industrial setting, where the billet temperature is lower in darker regions. In Figure 13, the

central top billet piece has remained a lower temperature than its surroundings, while it undergoes stirring. This shows that the heat conductive model accurately reflected the physics that would be expected during induction melting. Examining the velocity profile of the molten alloy in Figure 12, the velocity is higher at the top part of the crucible wall compared to the billet centre. This can be seen from the higher density of velocity streamlines at the crucible top edge, compared to in the centre. Therefore, it follows that the solid part of the billet would be eroded near the crucible wall before melting in the centre.

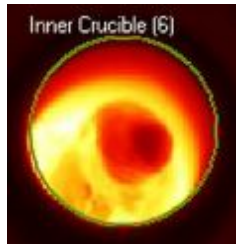


Figure 13: Thermal imaging: industrial induction melting

There are a number of factors which could contribute towards a difference between experimental and numerical results. Despite adopting effective material properties to account for strong convection, physics of the fluid flow were not modelled. Furthermore, various input parameters required for the model were not readily available or incomplete, such as temperature dependent material properties. Use of effective material properties and heat transfer coefficient are methods of model adjustment. This influences the output to reflect measured data, which could introduce error. Experimentally obtained temperature measurements are taken at a specific measurement spot, whereas the numerical result was an average temperature of the billet top face. Finally, a level of results discrepancy could be due to equipment sensitivity, which is inevitable.

5 Conclusions

In conclusion, a heat conductive model in COMSOL can accurately predict the thermal behaviour of a billet under induction heating and melting. Use of an effective thermal conductivity and specific heat capacity can account for rapid thermal transfer from a model, including convective fluid flow and eddy currents. Similarly, an artificially high effective heat transfer coefficient is helpful in modelling generalised heat losses. A model including fluid flow and convection was suitable for qualitative assessment of the velocity profile. However, the temperature behaviour for this model was not accurate. Further work will aim to develop a model which produces accurate temperature and velocity data, while accurately capturing the physics of melting and stirring.

Acknowledgements

The authors would like to thank Dr. Steve Leyland for his contribution towards this work from an industrial perspective.

In addition, they would like to thank Uni-Pol Group for their financial contribution towards this project, and the Swansea University MACH1 research group for the use of their laboratory equipment. Finally, the authors would like to thank the COMSOL Technical Support team for their advice and input regarding the model.

References

1. Rudnev V, Loveless D, Cook R, *Handbook of Induction Heating*, p.51. CRC Press, Online (2017)
2. Fisk M, Validation of induction heating model for Inconel 718 component, *International Journal for Computational Methods in Engineering Science and Mechanics*, **Vol. 12**, p.161-167 (2011)
3. Osborn H, Brace P, Johnson W, Cable J, Eagan T, *Induction Heating*, p.5. American Society for Metals, Cleveland (1946)
4. Boettinger W J, Kattner U R, Moon K -W, Perepezko J H, *DTA and Heat-flux DSC Measurements of Alloy Melting and Freezing*, p.35. National Institute of Standards and Technology, Washington (2006)
5. Mahendran K, Nagaraj S, Sridharan R, Gnanasekaran T, Differential scanning calorimetric studies on the phase diagram of the binary LiCl-CaCl₂ system, *Journal of Alloys and Compounds*, **Vol. 325**, p.78-83 (2001)
6. Raytek Corporation: A Fluke Company, *The Principles of Noncontact Temperature Measurement: Infrared Theory*, p.9. Fluke (2012)
7. ISS Ltd., *Endurance IR 2-Colour Infrared Thermometer Operating Instructions*, p.62. ISS Ltd. (2015)
8. COMSOL Group, *AC/DC Module User's Guide*, p.32-33. COMSOL (2018)
9. Wheeler H A, Formulas for the Skin Effect, *Proceedings of the I.R.E.*, **Vol. 30**, p.412-424 (1942)
10. Voller V R, Prakash C, A fixed grid numerical modelling methodology for convection-diffusion mushy region phase-change problems, *International Journal of Heat and Mass Transfer*, **Vol. 30**, p.1709-1718 (1987)
11. Bruyere V. *COMSOL Blog: Tips and Tricks for Modeling Induction Furnaces*. Available from: <https://uk.comsol.com/blogs/tips-and-tricks-for-modeling-induction-furnaces/> [Accessed 30th September 2020]
12. Frei W. *COMSOL Blog: How to Choose Between Boundary Conditions for Coil Modeling*. Available from: <https://uk.comsol.com/blogs/how-to-choose-between-boundary-conditions-for-coil-modeling/> [Accessed 30th September 2020].
13. De A, DebRoy T, A smart model to estimate effective thermal conductivity and viscosity in the weld pool, *Journal of Applied Physics*, **Vol. 95**, p.5230-5240.